A compact photoreactor for automated H_2 photoproduction: revisiting the (Pd, Pt, Au)/TiO_2 (P25) Schottky junctions

Pablo Jimenéz-Calvo [1,¥*], Mario J. Muñoz-Batista [2], Mark Isaacs [3,4], Vinavadini Ramnarain[5], Dris Ihiawakrim[5], Xiaoyan Li [1], Miguel Ángel Muñoz-Márquez [4], Gilberto Teobaldi [5,6], Mathieu Kociak [1], Erwan Paineau [1*]

*Corresponding Authors: pablo.jimenez-calvo@mpikg.mpg.de; erwan-nicolas.paineau@universite-paris-saclay.fr

[1] Université Paris-Saclay, CNRS, Laboratoire de Physique des Solides, 91405 Orsay, France
[2] Department of Chemical Engineering, Faculty of Sciences, University of Granada, Granada, Spain
[3] HarwellXPS, Research Complex at Harwell, Rutherford Appleton Lab, Didcot OX11 0FA, United Kingdom
[4] Department of Chemistry, University College London, 20 Gower Street, London, WC1H 0AJ, United Kingdom
[5] Institut de Physique et Chimie des Matériaux de Strasbourg (IPCMS), UMR 7504 CNRS, Université de Strasbourg, 67200 Strasbourg, France
[4] School of Science and Technology - Chemistry Division, University of Camerino, Via Madonna delle Carceri, 62032 Camerino, Italy
[5] Scientific Computing Department, STFC UKRI, Rutherford Appleton Laboratory, Harwell Campus, OX11 0QX Didcot, United Kingdom
[6] School of Chemistry, University of Southampton, Highfield, SO17 1BJ Southampton, United Kingdom
[¥] Department of Colloid Chemistry, Max-Planck-Institute of Colloids and Interfaces, Am Mühlenberg 1, 14476 Potsdam, Germany (present address)

ABSTRACT

The configuration and geometry of chemical reactors underpins the accuracy of performance evaluation for photocatalytic materials and, accordingly, the development and validation of thermodynamic and kinetic model reactions. The lack of accurate photonic, mass, and heat transport profiles for photochemical reactors hinder standardization, scale-up, and ultimately comparison between different experiments. This work proposes two contributions at the interface between engineering of chemical process and materials science: (A) an automated compact

stainless-steel photoreactor with 40 cm^3 and 65 cm^2 of volume and area, respectively, for hydrogen photoproduction as a model reaction and (B) the synthesis, characterization, and performance of TiO_2 Schottky junctions, using Pd, Pt, or Au nanoparticles (*ca.* 0.5, 1, 2wt.% loadings each) to validate the operation of the reactor. A photonic profile methodology is implemented to the studied reactor to obtain the local light absorption profile, opening up for evaluation of the local quantum yield calculation for the selected materials. A combination of transmission electron microscopy, (X-ray/ultraviolet) photoelectron/electron, energy loss/infrared spectroscopies, X-ray scattering, inductively coupled plasma atomic emission spectroscopy, and ultraviolet-visible spectrophotometry is employed to determine the distinctive surface and bulk properties to build structure-function correlations. The (Pd, Pt, Au)/TiO_2 Schottky junction exhibits H_2 production rates slightly higher than previous studies, with quantum yields almost 2-fold higher than reported values. These results, demonstrate that the proposed novel geometry of the photoreactor improves the photonic, heat, and mass profiles. An in-depth analysis of the Au plasmon was investigated coupling electron energy loss spectroscopy, UV-vis, and transmission electron microscope, resulting in insightful information about the Au NP mode at the TiO_2 interface.

Keywords: Photoreactor, photonic profile, Schottky junctions, co-catalysts, photocatalytic hydrogen

1. Introduction

Solar energy[1–4] is foreseen as a promising solution to the climate crisis due its highly abundant energy content.[5] Capturing only 0.04% of the 36000 TW irradiation that arrives to the Earth' surface would be enough to supply the global energy demand, *e.g.,* 28 TW by 2050.[5] The photoconversion of solar photons to energy on demand has reached maturity in some technologies, for example photovoltaics and/or concentrated solar power, but other tools are in current demand

and development. One promising pathway to solar light conversion is by storing it in chemical carrier molecules[6] (molecular dihydrogen, H_2), easy to transport and straightforward to integrate in the existing technological transformation processes.[7] Amongst the solar fuels, H_2 is one of the most attractive systems due to its high mass-energy content (142 MJ/mol), two- to three-fold higher than conventional fossil fuels, when used in direct combustion.[5] H_2 is mainly produced by steam-methane reforming but renewable sources and processes are starting to appear in the roadmap.[8] By using the trifecta of light, water, and a catalyst (TiO_2) in 1972 Honda & Fujishima photoproduced H_2 via water splitting. [9] Since then, there has been five decades of active research in the field, often referred by experts as one of the holy grails in physical-chemistry.[6]

Water splitting (WS), often referred as "artificial photosynthesis", corresponds to the dissociation of water into H_2 and oxygen (O_2). [10] Inspired by natural photosynthesis, the appeal of the artificial WS lies in the simplicity of its three components: light, catalyst, and water. A great promise of WS reaction is its low cost H_2 generation (energy carrier) while CO_2-free emissions. [11] Semiconductor materials, such as TiO_2 has been largely studied via photocatalysis and other methods. [12–15]. The photocatalytic path of WS comprises three general but sequential steps: a) TiO_2 absorption of light, generating an exciton (electron/hole pairs), b) the photogenerated holes (h^+) oxidize adsorbed water given protons (H^+) and O_2, and c) the H^+ react with photogenerated electrons (e^-) to form H_2.[6] Such sequential steps are represented in the following reactions 1-3.

$$TiO_2 + hv \rightarrow e^- + h^+ \text{ (exciton formation) (1)}$$
$$H_2O_{(l)} + 2h^+ \rightarrow 1/2O_{2(g)} + 2H^+ \text{ (water oxidation) (2)}$$
$$2H^+ + 2e^- \rightarrow H_{2(g)} \text{ (proton reduction) (3)}$$

WS is an endothermic reaction that requires a potential of 1.23 V to occur. However, energy losses are unavoidable in practice due to dispersion caused by the ionic strength of the medium or kinetic

overpotential. As a result, the true potential required to effectively split a water molecule ranges between 2 and 2.4 V.[16] Thereby, a common practice to surpass such thermodynamic limitation in WS photocatalysis is the use of a sacrificial agent (SA), allowing the study of one single evolved gas in detailed. Because the nature of H_2 evolution reaction (HER) and O_2 evolution reaction (OER) differs, it is necessary to select a sacrificial agent based on its capacity for reduction or oxidation. [17,18] For the HER case study, an electron donor must be used for two reasons: to scavenge the photogenerated holes (enhancement of charge separation) and, if O_2 is present in the reaction medium, to consume it (limiting the back reaction). Common SA for HER are alcohols and amines, among which the most used are methanol, ethanol, and triethanolamine. [19,20] We selected methanol in this study. The reader interested in the details of the mechanistic insights can refer to Guzman *et al* work. [11]

Heterogeneous photocatalysis research into the HER requires the use of a suitable photochemical reactor along with the assistance of a SA. It is noteworthy to say that the scaling-up of photocatalytic H_2 production has not reached a sufficient technological readiness level (TRL) due to a dual bottleneck: (A) efficient, abundant, recyclable, and low-cost catalysts and (B) a scalable, reproducible, and easy to handle reactor with a homogeneous photonic/heat/mass profile. Unfortunately, researchers have not yet developed photo catalytically active materials from cheap, abundant sources with the required ~10% solar-to-hydrogen energy conversion capacity[21,22] nor have we constructed a standard photochemical reactor of efficient photonic/heat/mass transfers with low losses. Therefore, the rational design of advanced photocatalytic systems has been the center of attention for several decades. However, the development of batch, scalable, and compact photoreactors has progressed more slowly compared with the advances made in photocatalytic materials discovery.[23] The design of compact and transportable photoreactors comprising

favorable properties (efficient local radiation/photonic flux, high photon absorption, homogeneous heat transfer, constant temperature during reaction, low volume, low mass of catalyst, good particle distribution) is of paramount importance for the TRL ascend [24] towards achieving unprecedented thermodynamic and kinetic efficiencies. Of equal importance is the capability to perform operando and *in-situ* tests [25–27], for better informed developments in the field. In this context, development of improved and better standardized photoreactors could reactivate interest and efforts in this perhaps the currently overlooked sub-field of photochemical engineering.

In terms of the photocatalytic materials design, multi-phase heterostructures in different organic/inorganic/metals (M) combinations have proven to surpass the efficiencies of their individual semiconductor (SC) components by modifying optical, electronic, morphological, structural, bulk, and surface properties.[28–30] Numerous multi-component composites have been reported and further progressed the semiconductor photocatalysis field. Regardless of these efforts, the benchmark material remains titanium dioxide (TiO_2), despite its wide band gap, *ca.* 3.2 eV,[15] hindering the utilization of an important part of the solar spectrum, namely the visible one.[31] For that reason, titania-based materials have been rationally designed following different strategies – with the aim of improving visible-light capture properties. Examples include deposition of noble & coinage M (Schottky junction formation),[32–41] doping with impurities[42] (cation, anion, co-doped, and co-alloyed), coupling with medium or small band gap SCs (staggered/Z-scheme heterojunction formation),[21,28,29,43] and dye grafting[44,45] (surface activation and/or photosensitization).

Among the different TiO_2 band gap engineering modifications,[28,29,46,47] Schottky junction formation is particularly attractive because it exploits the use of deposited metal (M) nanoparticles (NPs) onto a substrate SC with a physico-chemical contact to form an intimate interface. This

composite structure exploits first, the co-catalytic active sites and second, the electron pump functionalities, driven largely by electronic properties. A third functionality can be expected in cases where the M NP of choice has a surface plasmon, defined as the collective coherent oscillation of free electrons upon irradiation of a specific photon energy.[48] In photo(electro)catalysis M/SC combinations have been widely used due to their vast performance augmentations delivered by the M NPs, bringing significant improvements (≥10 fold) compared to the SC alone.[49] Purely electrocatalytic metal activity has been elucidated to form a volcano plot relative to the standard free energy of adsorption assuming a Langmuir adsorption isotherm.[50,51]

The present work highlights two contributions in interconnected sub-fields: (A) a newly designed compact photoreactor (**Fig. 1a**) for automated HER in the presence of a sacrificial agent with frontal irradiation (engineering of chemical processes) and (B) synthesis, characterization, and performance of TiO_2 Schottky junctions, using Pd, Pt, or Au nanoparticles (*ca.* 0.5, 1, 2wt.% loadings each) to validate the operation of the reactor (materials science). Our hope is to further stimulate the design of novel compact reactors and accelerate the TRL-development for photo(electro)catalysis. Automated data acquisition and H_2 quantification at controlled intervals is made possible due to the inclusion of an in-line gas chromatographer into the experimental configuration with defined parameters. Details on the setup are provided in **Experimental section**. The circular wall geometry, in contrast to other reactors[47,52,53], is conceived to avoid accumulation of particles on the corners, which guarantees continuous and homogeneous circulation of the NPs. A flat compartment at the bottom of the reactor (the width of a magnetic stirrer diameter – 0.5 cm) prevents obstructions to the vortex flow and enables sufficient convection to maintain a homogeneous suspension of NPs. Both geometrical choices are chosen

to increase the photon-NP impact probability when entering from the quartz window. A second source of NP transport is included in the form of a cross sectional vortex from the N_2 line, entering at the top right-hand side of the reactor. When determining the thickness (or depth) of the cylinder, a compromise is required between suspended NPs concentration and their passage into the quartz window entrance, the gateway of the incoming photons. Further to this work, a parametric study on stirring speed, NPs concentration, sacrificial agent concentration/nature, N_2 flux rate, and monochromatic lights should be envisaged.

2. Experimental section

2.1.Chemicals

AEROXIDE ® titanium dioxide P25 (TiO_2, 99%, Evonik Industries), Palladium (II) nitrate hydrate ($N_2O_6Pd*xH_2O$, ≥99.9%, Sigma Aldrich), Hexachloroplatinic acid hexahydrate ($H_2PtCl_6*6H_2O$, ≥37.5% Pt basis, Sigma Aldrich), Chloroauric acid trihydrate ($HAuCl_4*3H_2O$, ≥99.995% trace metal basis, Sigma Aldrich), sodium borohydride (≥98%, Sigma Aldrich), methanol (CH_3OH, ≥99.6%, Sigma Aldrich), ethanol (CH_3CH_2OH, ≥96%, Sigma Aldrich) were used without further purification.

2.2.Synthesis: noble metals anchoring onto TiO_2

(Pd, Pt, Au)/TiO_2 P25 samples were prepared by chemical reduction of the three different listed metal precursors.[54] The TiO_2 P25 support (350 mg) without further purification nor modification was dispersed in a methanol/ethanol mixture (91/9 v/v, 55 mL) with a sonicator bath (120 W, 45 kHz) for 30 min, using 50% of the maximum sonication power. A calculated volume of a methanol/ethanol solution of the listed metal precursors solutions (15 mmol L^{-1}) was added to

achieve the chosen loadings, *i.e.,* 0.5, 1, and 2 wt.%. Suspensions were sonicated for 5 min, whereupon 5 mL of a fresh methanol/ethanol solution of $NaBH_4$ (10 mole fold higher than the initial precursor concentration) was added to guarantee full reduction of the cation metal.

2.3.Materials characterization

High-resolution transmission electron microscopy (HRTEM), TEM observations on individual deposited nanoparticles were performed on a JEOL1400 microscope operating at 80 kV. Samples were prepared according to a previously reported method.[55] Dilute aliquots of M/TiO_2 were prepared at 1 mg L^{-1} in ethanol. A drop of this mixture was deposited on a copper grid coated with carbon layer and dried at room temperature. The morphological parameters were measured over 200 individual particles using Fiji software.

The Energy Dispersive X-Ray Spectroscopy (EDX) and elemental mapping were both carried out using a JEOL JEM 2100F microscope with an EDX detector. 1 mg of sample was dissolved and sonicated for 5 min with ethanol in a flask and 1µL of the solution was deposited on a copper grid. The quantitative results were obtained by data treatment using Analysis Program.

Elemental analyses of the Schottky junctions were performed using ICP-AES. The limit of detection of the instrument was 0.1-0.2 mg L^{-1} for the chosen metals. Quantitative analysis of the noble metal component of the M/TiO_2 composites allowed the calculation of deposition yield which ais defined as the ratio between the actual deposited mass of the specific metal (deduced from ICP-AES analysis) and the mass of metal introduced during the deposition step (**Table 1**).

X-ray scattering (XRS) measurements were carried out on a Mo rotating anode generator (Rigaku Corp., Japan) equipped with a multilayer mirror (Osmic) delivering a monochromatic beam with

incident wavelength $\lambda_{Mo,K\alpha}$ = 0.711 Å. Two-dimensional XRS patterns were collected on a MAR345 image plate detector (marXperts GmbH, Germany, pixel size = 150 μm) placed at a distance of 150 mm from the samples. Powder samples were filled into borosilicate capillary tubes (WJM-Glas/Müller GmbH, DE) that were mounted on a goniometer head. Typical exposure time was 900 s. Scattered intensity I as a function of the scattering vector modulus Q ($Q = 4\pi/\lambda \sin(\theta)$ where 2θ is the scattering angle) is obtained by angular integration over the 2D scattering patterns using homemade software. The Scherrer equation was used for the determination of the average crystallite size of the nanoparticles onto the support:

$$L = K\lambda/\beta \cos\theta$$

with λ the incident wavelength and β the Full Width at Half the Maximum of the X-ray scattering peak (in radians) at a Bragg angle q. *K* is defined as the shape factor and is taken to be 0.9 for spherical-like particles.

Fourier-transform infrared spectroscopy. FTIR spectra were recorded on dry sample powders using a Nicolet iS50 (Thermo Scientific) spectrometer equipped with a KBr beam splitter and a DTGS/KBr detector. The transmission measurement in the range 4000−800 cm^{-1} was performed by averaging 200 scans at a resolution of 4 cm^{-1}. Transparent pressed pellets were prepared by mixing about 1.5 mg of dry powder sample with 150 mg of transparent KBr, to guarantee 1 wt. % of sample inside the final pellet.

Diffuse Reflectance UV-Vis Spectroscopy (DRUVS) was recorded on a Varian Cary 5E spectrophotometer from 300 to 650 nm. DRUVS spectra were converted into Kubelka-Munk units according to $F(R)= (1-R_d)^2/2R_d$, where $R_d= R_{sample}/R_{BaSO4}$, ($BaSO_4$ as the standard). For band gap calculation, a Tauc plot was used and considering TiO_2 as indirect SC.

XPS analysis was performed using a Kratos Axis SUPRA XPS fitted with a monochromated Al Kα X-ray source (1486.7 eV), a spherical sector analyzer and 3 multichannel resistive plate, 128 channel delay line detectors. All data was recorded at 150 W and a spot size of 700 x 300 μm. Survey scans were recorded at a pass energy of 160 eV, and high-resolution scans recorded at a pass energy of 20 eV. Electronic charge neutralization was achieved using a low energy electron flood gun. Filament current = 0.27 A, charge balance = 3.3 V, filament bias = 3.8 V. All sample data was recorded at a pressure below 10-8 Torr and a room temperature of 294 K. Data was analyzed using CasaXPS (v2.3.19PR1.0). The energy shift due to electrostatic charging was subtracted using the carbon adventitious signal, *i.e.,* the C 1s peak located at 284.8 eV. Peaks were fit with a Shirley background prior to component analysis with the appropriate experimental sensitivity factors of the normalized photo ionization with modified Wagner factors.[56]

UPS analysis was performed using a Thermo NEXSA spectrometer fitted with a He (I) and He (II) lamp and dual neutralization flood gun. Such setup was equipped with a CLAM4 (MCD) hemispherical electron analyzer. Samples were drop cast from isopropanol onto copper foils prior to analysis. Spectra were recorded using a pass energy of 5 eV, a positive bias of 30 V to avoid interference of the spectrometer threshold, a current of 50 mA and an energy step size of 0.1 eV.

Plasmon properties of Au NP@TiO_2 were studied by electron energy loss spectroscopy (EELS) in a modified NION monochromated Cs-corrected HERMES200 Scanning Transmission Electron Microscope (STEM) fitted with a MerlinEM direct electron detector (Quantum DETECTORS). In this work, the experiments were performed at 60 kV, at a condenser convergent semi angle of 10 mrad with a typical EELS energy resolution (FWHM of ZLP) of 20 meV.

2.4.Photocatalytic tests

The photocatalytic activities of the (Pd, Pt, Au)/TiO_2 P25 Schottky junctions were evaluated against H_2 evolution reaction (HER) from methanolic aqueous solution (30% v/v) as sacrificial agent in a newly compact photoreactor setup (**Fig. 1a**). H_2 production was performed in a compact stainless-steel photoreactor with 40 cm^3 and 65 cm^2 of volume and area, respectively using a quartz fused window (loss light intensity ≤5%) of 50 x 3 mm diameter and thickness containing 12 mL of methanol and 28 mL of Mili-Q deionized water. The 500 W Hg arc lamp from LOT Design (15.5 mW cm^{-2}, **Fig. S1**) was linked with a water filter circulating continuous tap water of 70 cm length allowing to pass 250-1000 nm to reduced unwanted heat increased and avoid thermal catalytic effect. The irradiance of such lamp was measured with a spectroradiometer (ILT950-UV-NIR, International Light Technologies). Prior to any experiment, residual oxygen was removed by nitrogen flushing. The photocatalytic tests were performed by suspending 40 mg of catalyst in 30% v/v of methanolic aqueous solution under continuous nitrogen flow at 60 mL min^{-1} and with mechanical stirring at 400 rpm. The reaction products were automated quantified online every 120 s by a μGC (990 model, Agilent) equipped with a thermal conductivity detector, comprising a 10% error. The channel for H_2 quantification was using nitrogen as carrier gas flushing into a molecular sieve 5A SS (10m x 0.25mm x 30 μm). The injection system contained a pre-column and a backflush system for filtering undesirable humidity and separate more accurately the interest product while protecting the columns lifetime. A calibration curve was done using two Air Liquide gas standards with 1 and 99.9% concentration of H_2.

Stability and recycling ability were conducted using photocatalytic test of 3h each cycle. The protocol consisted of after each photocatalytic cycle, the photocatalyst was filtered, washed, and dried. Then the photocatalyst was re-used and the experiment initiate under the same initial experimental conditions. Parametric optimization studies and blank tests were performed under

the same principle, with the slight difference of being recorded for only 90 min.

2.5. Photonic profile description and quantum yield calculations

The photonic profile methodology is described in detail in the Support information (SI, **Fig. S2**). The local volumetric rate of photon absorption is extracted from the photonic model.

The latest equations from the photonic model are related to intensity. Such equations consider linear intensity profiles inside each spatial mesh cell (an approximation which has increasing accuracy as the finite, delta r and z elements go to zero). The local volumetric rate of photon absorption ($e^{a,v}$) was calculated at each $r-z$ point of the reactor according to:

$$e^{a,v} = \int_{\lambda} \kappa_{\lambda}(\underline{x}) \cdot \int_{\Omega=4\pi} I_{\lambda,\underline{\Omega}}(\underline{x}) d\Omega \, d\lambda$$

From the latter equation, the absorbed intensity of each sample can thus be extracted enabling the quantum yield equation application as follows:

$$\eta_q(\%) = 100 \times \frac{2 \times r \ (\text{mol m}^{-3}\text{s}^{-1})}{< e^{a,v} > \ (\text{Einstein m}^{-3}\text{s}^{-1})}$$

This equation considers two electrons transfer to reduce two protons into one H_2 molecule.

3. Results and discussion

Therefore, the implementation of a photonic model is of great use for two reasons: a) evaluate the photoreactor photonic transfer efficiency and b) to combine such functionality with the material's light absorption to obtain quantum yields (Q.Y.). The light absorption capacity of the photoreactor is evaluated through a photonic model (well described elsewhere)[25] and implemented for our photoreactor to understand process efficacy.

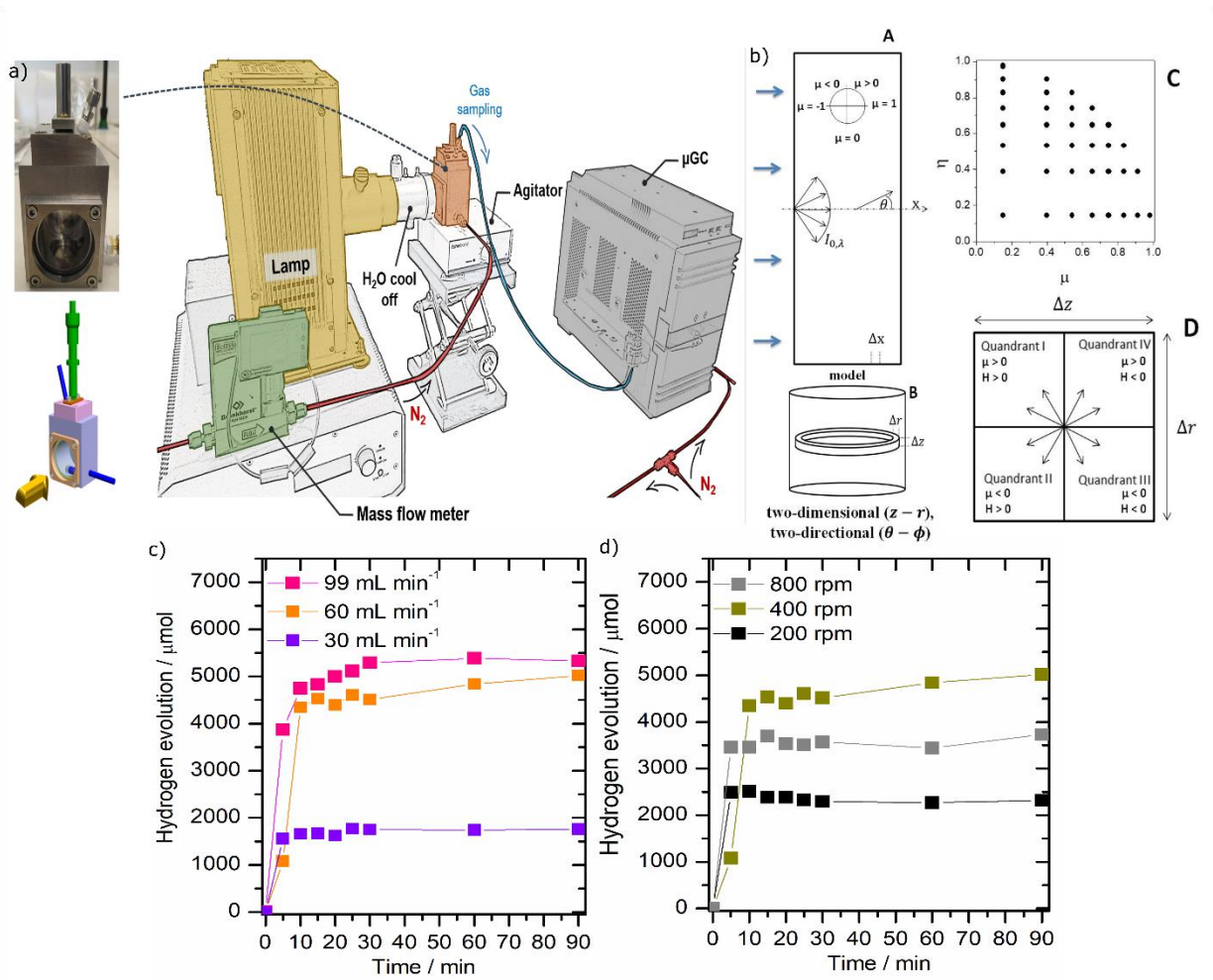

Figure 1. a) Compact photoreactor and its setup accessories. **b)** Photonic local profile of the reactor showing the one-dimensional/one-directional radiation model (A) and two-dimensional, two-directional radiation (B-D). (B) Representation of the r and z spatial mesh discretization of the photoreactor, (C) Directional mesh for the Quadrant I and (D) representation of quadrants of the spatial cell. Hydrogen evolution of 0.5%Pd/TiO_2 selected catalyst when optimizing operational parameters **c)** nitrogen inlet flux **d)** agitation speed of the magnetic stirrer.

In short, the radiative transfer system (RTE, equation S1) is proposed assuming a set of defined physical properties and geometry conditions (see S1). The model combines the optical properties of the photocatalyst suspensions at different concentrations using the discrete ordinate method (DOM) in the rectangular spectrophotometer reactor. The reactor is considered as infinite plane parallel medium with azimuthal symmetry, with one-dimensional and one-directional radiation transport model to solve the RTE (**Fig. 1b) A**). To apply the DOM tool to transform the integro-differential equation S1 into a system of algebraic equations (possible to solve numerically) our

reactor configuration requires the use of a cylindrical two-dimensional (r-z variables) and two-directional ($\theta - \phi$ variables) model of the photoreactor radiation field (**Fig. 1b) B-C**). The net radiation intensity at each $r - z$ point of the reactor is now represented using a discretized spatial mesh having two angular-related coordinates $\mu = \cos(\theta)$; $\eta = \cos(\phi)$. Fig. 1b) C displays μ; η unitary, basal projection(s) in a quadrant of the space around a $r - z$ point calculated using the S16 method (discretization division of octants comprising eight progressing levels for each of the two direction cosines).[57] Obtaining intensity at each point of the reactor requires dividing the space into 4 quadrants as depicted in **Figure 1b) D** and the measurement of the incident light intensity at the boundary (liquid surface) using actinometry.[58] According to the Duderstadt and Martin recommendation and their proposed numerical procedure[58], the finite difference and DOM was derived directly from the radiation balance for each mesh reactor (**Fig. 1b) D**). As a result of solving the algebraic system (elucidated in S1), the local volumetric rate of photon absorption ($e^{a,v}$) is calculated at each $r - z$ point of the reactor according to the integral:

$$e^{a,v} = \int_{\lambda} \kappa_{\lambda}(\underline{x}) \cdot \int_{\Omega=4\pi} I_{\lambda,\underline{\Omega}}(\underline{x}) d\Omega \, d\lambda$$

Details of the RTE and DOM approaches are given in supplementary information section.

The commissioning of this compact reactor is assessed by revisiting the well-studied Schottky junctions, in the form of benchmark TiO_2 (P25) containing noble M (Pd, Pt, or Au) NPs for validation. Parametric optimization studies were carried out to find the best operational conditions. The catalyst 0.5%Pd/TiO_2 was selected to find the optimal nitrogen flux and agitation speed of the magnetic stirrer. **Fig: 1c** shows the H_2 evolution while testing three different nitrogen fluxes, 30-, 60-, and 99-mL min^{-1}. Thus, 30 mL min^{-1} of flux shows the lowest H_2 production rates compared

to the 60 and 99 fluxes. Between 99 and 60 mL min^{-1} are very similar, which allows to conclude that 60 mL min^{-1} is the best experimental compromise with lower consumption of nitrogen gas too. **Fig. 1d** shows the H_2 evolution when agitation speed is modified at 200, 400, and 800 rpm. The latter results in low evolution for 200 and 800 rpm. Therefore, the best compromise was obtained for 400 rpm. Several reasons can be argued, but light scattering and continuous homogeneity may be the key reasons of this optimal behavior. Based on these results, 60 mL min^{-1} of nitrogen flux and 400 rpm of agitation speed were the chosen values for further photocatalytic tests due to the well-associated photon capture and chemical conversion compromise. The necessary blank tests were also tested (**Fig. S2b**) using the conventional methanolic solution (30%) in Milli Q water in all cases.

(Pd, Pt, Au)/TiO_2 P25 composites are synthesized via two-step chemical reduction methodology (**Fig. 2**, see **Experimental section**). For each anchored M onto TiO_2, three loadings, *i.e.,* 0.5, 1, and 2 wt. % are implemented, standing for M0.5, M1, and M2, respectively, where M can be: Pd, Pt, or Au.

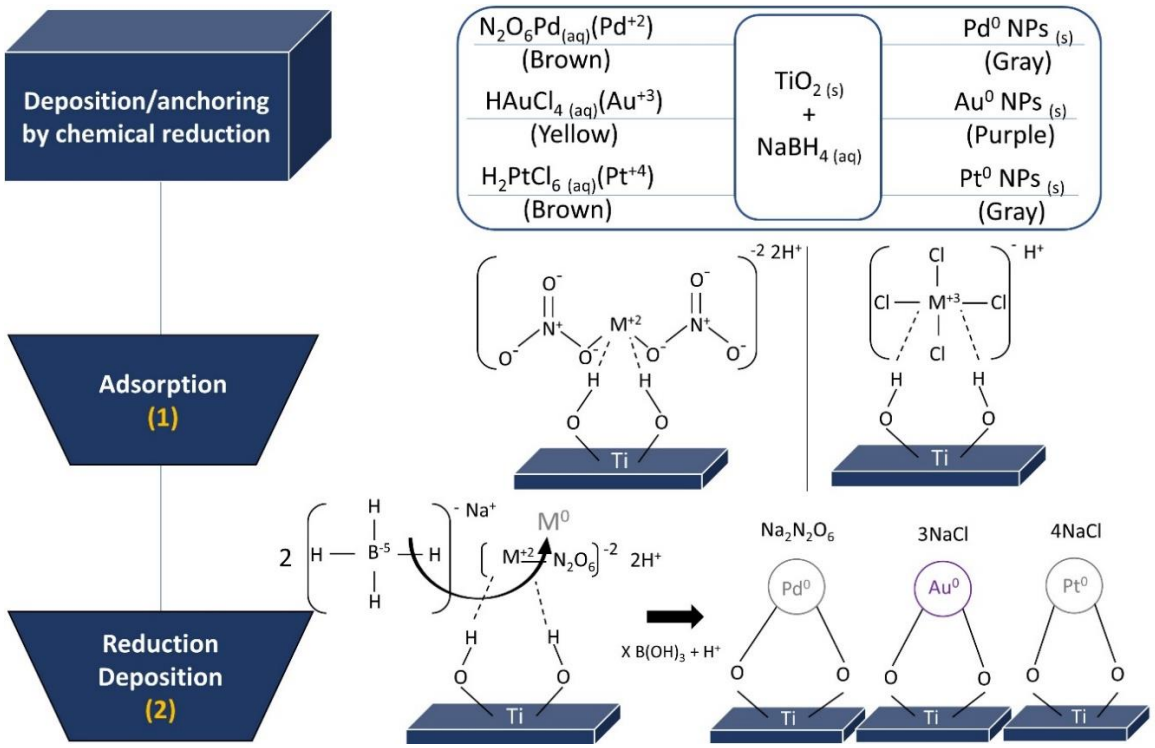

Figure 2. Illustrative scheme of the two-step chemical reduction deposition mechanism: adsorption of the M precursors followed by chemical reduction during the anchoring step.

Elemental analysis performed by inductively coupled plasma atomic emission spectroscopy (ICP-AES) indicates that the chemical reduction method ensures relatively high deposition yield, the resulted M content is also reported (**Table 1**), while HRTEM analysis reports a good distribution of controlled size for each M NP systems (**Fig. 3**). The metal deposition yield onto TiO_2 ranges from 67 to 81% for all composites. It should be noted that the Au deposition yield (72-80 %), is higher than for Pd (70-74%) and Pt (67-71%), however this difference may be considered to be relatively minor, ensuring a reliable comparison for the photocatalytic H_2 production for each system.

Table 1. Metal content, deposition yield, and anatase crystallite size of all the Schottky junction materials.

Sample	M content wt.%	Deposition Yield %	Anatase (101) nm
Pd0.5	0.37	74±2	10.0±0.4
Pd1	0.72	72±2	10.2±0.4

Pd2	1.40	70±2	10.0±0.4
Pt0.5	0.34	68±2	10.2±0.4
Pt1	0.67	67±2	10.5±0.4
Pt2	1.41	71±2	10.1±0.4
Au0.5	0.38	76±2	10.1±0.4
Au1	0.81	81±2	10.1±0.4
Au2	1.3	72±2	10.4±0.4

The HRTEM micrographs in **Fig. 3a-i** show the nine Schottky junction composites, three for each metal with equivalent loadings, namely Pd0.5, Pd1, Pd2 (**a-c**), Au0.5, Au1, Au2 (**d-f**), and Pt0.5, Pt1, Pt2 (**g-i**). These images illustrate the typical grains of TiO_2 P25 with particulate diameters spanning a few tens of nm. Regarding the metal loadings, Pd, Pt, and Au NPs display a spherical morphology although a minor population of cylindrical NPs is also present for Pt. Pd (3.6-4.3 nm) and Pt (2.2-2.9 nm) particle size is found to exhibit a monomodal distribution, essentially independent of metal loading across the range of loadings prepared in this work (**Fig. S3**). Au/TiO_2 composites however, present a slight discrepancy in NP size (3.1-5.0 nm), with increasing loading. As we increase the loading from 0.5, through 1 and 2 wt.%, we observe an increase in particle size from 3.1 nm, through 4.3 nm, and up to 5.0 nm (**Table S1**). One can conclude that there is a quasi-linear trend of the Au NPs size by doubling and/or quadrupling its content, while the variance in particle size (**Table S1**) suggests reproducible growth of the Au NPs.

The Pd/TiO_2 binary samples display a relatively lower coverage along their surfaces than Au/TiO_2 homologues, and the distribution is preferentially located in specific regions. The Pd/ (0.5, 1, and 2 wt.%)/TiO_2 materials yield an average size of 4.1, 3.6, and 4.3 nm (**Table S1**), evidencing that the method allows to maintain a narrow range of NPs sizes independently of the M content. Compellingly their associated standard deviations have 1.4-1.6 nm (**Table S1**) values, confirming a high degree of dispersity of the NPs sizes, *i.e.,* ranging from 1 to 7 nm, for the three loadings. A

minor population of NPs (8 and 9 nm) are presented, possibly in charge of the high deviation value corroborating also the inhomogeneous coverage. The Pt/TiO_2 junctions display a low and inhomogeneous coverage along the TiO_2 grains. Pt presents a particularly narrow NP size distribution with 2.2, 2.9, and 2.5 nm (**Table S1**) with the smallest standard deviation ranging from 0.6 to 1.1 nm. Such average NPs sizes are statistically equivalent, but their low deviation evidences the consistency on the NPs size in all the three composites, *e.g.,* 2.2-2.9 nm. Furthermore, one can conclude that the chemical reduction method for the junction system is consistent independently of the precursor used due to the monomodal particle size distributions for the three metals.

EDX mapping analysis of 2 wt.% of Ti, O, and the case study M atoms (**Fig. 3j-l** and **Fig. S4a-c**) exhibited good distribution, with Ti and O presence as the predominant ones, as expected. In fact, Pd, Au, and Pt seem well-dispersed over TiO_2 NPs, which in principle increases the co-catalytic encounters with the substrate molecules of the reaction medium. Regarding, the associated atom spectra (**Fig. S4 a-i**), they all exhibited Ti, O, and the expected case study M. Interestingly, a descending trend of the intensity peak signal for the studied metals (Pd, Au, and Pt) while diminishing the metal loading, as expected. Due to low signal of each M, close to noise to ratio thus detection limit, quantification was not thus possible.

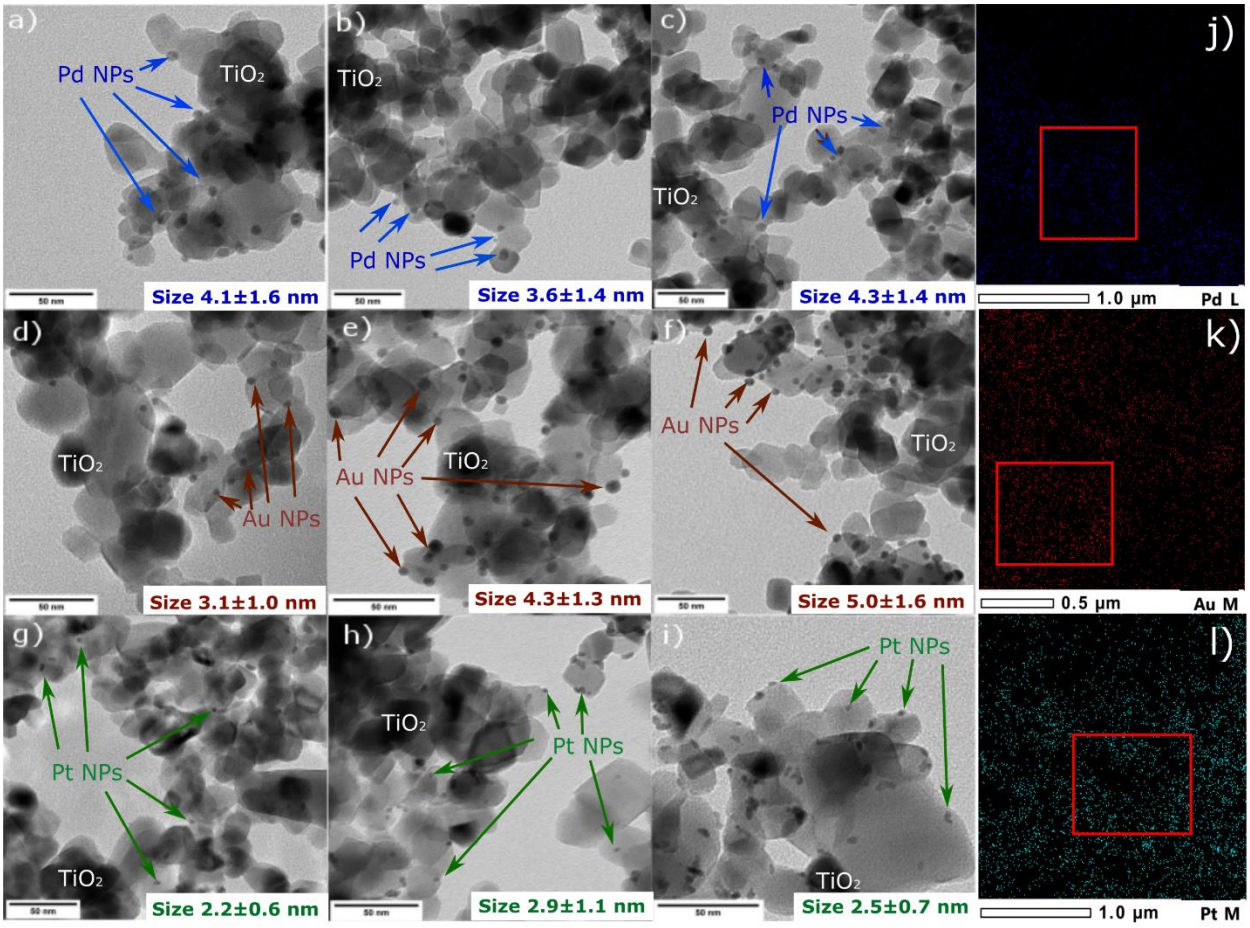

Figure 3. HRTEM images of the 0.5, 1, and 2 Pd/TiO_2P25 (a-c), Au/TiO_2P25 (d-f), and Pt/TiO_2P25 (g-i). EDX elemental mapping of 2 wt.% of j) Pd/TiO_2 k) Au/TiO_2 l) Pt/TiO_2.

FT-IR spectroscopy is used to probe the influence of the three anchored Ms onto TiO_2 surfaces in different loadings. FT-IR spectra of all composites (Pd, Au, and Pt) and reference (bare TiO_2) (**Fig. S5**) exhibit the characteristic peaks of TiO_2. The major broad absorption band extending from 3000 to 3600 cm^{-1} observed in all 10 samples is attributed mainly to the asymmetrical and symmetrical stretching vibration of surface hydroxyl groups (O-H) but also to, a lesser extent, to physisorbed water species.[59] A doublet with similar intensity is present at ≈1620 cm^{-1} and ≈1400 cm^{-1} for all samples. The absorption band located at ≈1620 cm^{-1} is assigned to the bending vibration of Ti-OH distorted by the adsorbed water molecules.[60,61] The absorption band located at ≈1400 cm^{-1} can be related to the accompanied by two weak bands at ≈2920 and 2850 cm^{-1}, due to the vibrational modes of organic species.[61] In general, the recorded spectra between the composites and the

reference do not exhibit significant differences. Nonetheless, a slight shift to lower wavenumber after metal loading can be seen and tentatively related to hydroxyl bond weakening due to H-bond formation with the metals. Overall, these results suggest that the deposited M NPs do not drastically influence the TiO_2 lattice.

X-ray scattering (**Fig. S6**) of Schottky composites, a pristine TiO_2, plus calculated XRS diagrams of pure anatase and rutile phase uncover the structural properties of the composites. The diffractograms of TiO_2 P25 display well-resolved Bragg peaks corresponding to a mixture of anatase and rutile,[62] as expected. The scattering from TiO_2 particles is not affected by the choice of metal nor loading, suggesting that the formation of the M/Schottky junctions does not alter the crystal structure of bulk TiO_2. This is confirmed by estimating the coherent scattering length for the anatase crystallographic phase (101 plane), using the Debye-Scherrer equation. The average crystallite size (**Table 1**) for anatase (10.0-10.6±0.4 nm) does not vary by significant amount, while differences due the presence of metal crystallites may not be detected due to the low M concentration (according to HRTEM) since the metal NP diameters are not large enough to form Bragg peaks from Mo K_α X-rays.

UV-vis spectra of all samples (**Fig. S7**) display the typical absorbance maximum in the UV/blue range of TiO_2, ($\lambda_{absorption}$ = 386 nm)[63], equivalent to an approximate apparent band gap of 3.2±0.1 eV deduced by a Tauc plot. Au/TiO_2 composites alone produce a clear maximum centered at *ca.* 530 nm,[64,65] attributed to the well documented surface plasmon resonance (SPR) of Au NPs. The SPR plasmon intensity correlates with metal loading, while an accompanying redshift in the peak maximum. Pt and Pd NPs do not exhibit an SPR in the visible range.

Surface analysis of the metal NPs was performed using X-ray photoelectron spectroscopy, to elucidate metal speciation and probe local chemistry. Survey spectra (**Fig. S8**) reveal the composites to be entirely Ti, O, C and the relevant metal. High-resolution scans of the Pd 3d, Au 4f and Pt 4f regions indicated an entirely metallic identity for all 9 materials. Pd 3d (**Fig. 4a**) and Au 4f (**Fig 4b**) scans may be characterised by the presence of single spin-orbit doublet (Pd $3d_{5/2}$ + Pd $3d_{3/2}$ and Au $4f_{7/2}$ + Au $4f_{5/2}$) of asymmetric character and were fit using modified Voigt-type lineshapes modelled from bulk metal standards. Platinum 4f (**Fig 4c**) also reports a single oxidation state of metallic, asymmetric peaks – though deconvolution is somewhat complicated by the presence of an energy loss feature from the Ti 3s photoemission. Quantification of the photoemission peaks revealed similar trends regarding surface:bulk ratios (**Fig. S9**) – that of a general inverse proportionality typical of nanoparticles on a surface.

UPS spectra (**Fig. S10**) allow determination of both valence band maximum (VBM) and work function (WF, **Fig. 4e**), whilst knowledge of the material band gap (deduced by Tauc plot) makes possible the calculation of the conduction band minimum (CBM), providing an energy band alignment diagram (**Fig. 4d**) including the oxidation-reduction potentials extracted from the Pourbaix diagram.[66] TiO_2 is not influenced optically nor structurally by anchoring of the M clusters. The resulting band gap indicates this clearly since all composites exhibit 3.2±0.1 eV value (**Fig. S7**). The first trend found is the significant VBM difference (0.23 eV) between pristine (-3.48 eV) and reduced TiO_2 (-3.25 eV), presumably due to the loss of surface hydroxyls and oxygen vacancies after treatment with $NaBH_4$ in excess coupled with the sonication process. For all of the M/TiO_2 composites a concomitant increase in the VBM/CBM edge with loading is observed, following the same argument of hydroxyl loss due to anchorage. The only exception to this trend is Au0.5 though this can be attributed to the less homogeneous Au nanoparticulate structural

parameters, known to impart complex influence upon electronic properties.[67] In all cases, the inclusion of M NPs into the TiO_2 SC markedly enhances the VBM/CBM levels, confirming the M/SC interface.[13] Moreover, the resulting SC band edges can be evaluated against water redox potentials – all samples in principle can undergo the water oxidation, though photo reduction may be easier for the samples with higher M loading (2wt%) since these have higher VBMs relative to H^+/H_2 potential values compared to the low M loading samples. However, provided the M/SC interface junction is formed, some additional charge carrier pathways can exist and contribute to surpassing the overpotentials (Schottky barrier) and promote HER. This can be through an electron pump from the CB of the SC to the M NP or via hot electron injection from the SPR active Au NP to the TiO_2 CB.[68] The WF results (**Fig. 4e**) are firstly compared to the theoretical values of TiO_2 (4.6-4.7 eV), Au (5.10-5.47 eV), Pd (5.22-5.60 eV), and Pt (5.12-5.93 eV)[69,70] given the classic efficacy stated in the volcano plot Pt>Pd>>Au. The WF-value recorded for Pd and Pt are comparable to the theoretical values, while the one for Au is marginally higher than expected; potentially the result of differences in strong metal-support interaction between the Au NPs and the TiO_2 support.[71] In the case of unmodified TiO_2, the WF values are 0.6-0.7 eV higher than those determined theoretically. However, the relative difference between the samples implies a stability of the overall electronic configuration during the reduction process. The Au WF values are above those for the Pt and Pd junctions. However, in general, the differences (0.1 eV) between the different M loadings are small, pointing to an overall electronic stability.

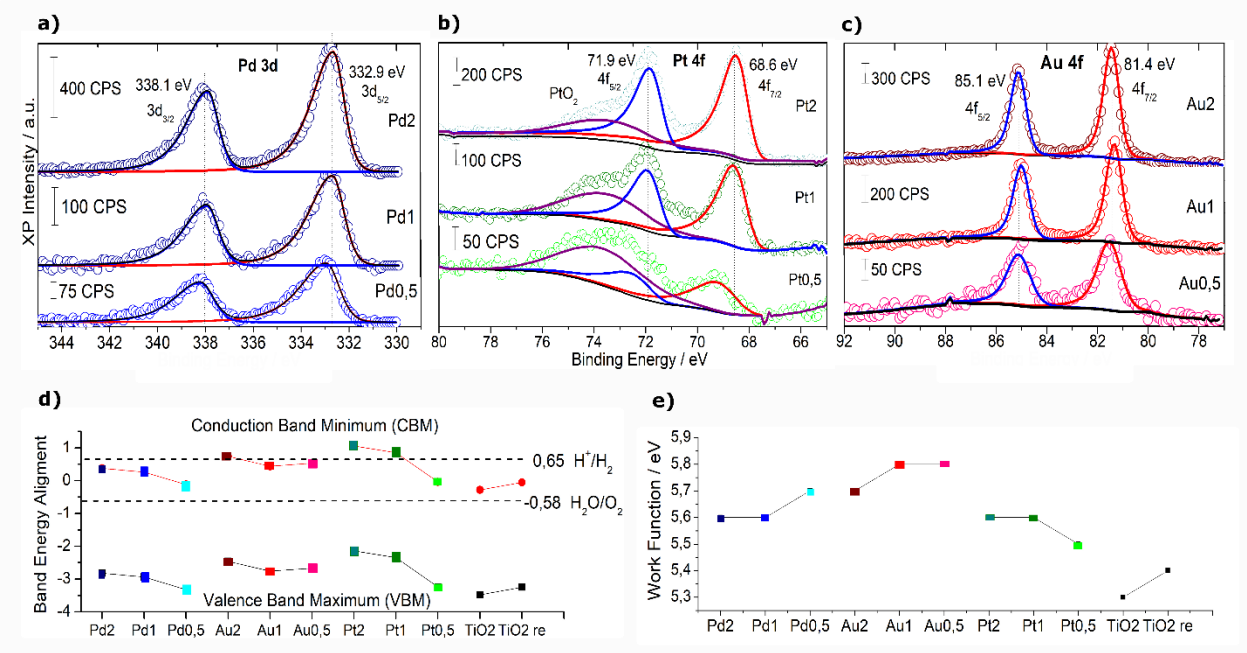

Figure 4. XPS spectra a) Pd 3d b) Pt 4f and c) Au 4f d) Band alignment diagram by coupling UPS and UV-vis e) Experimental work function of the 0.5, 1 and 2 wt.% (Pd, Pt, and Au)/TiO_2 composites.

The (Pd, Pt, and Au)/TiO_2 junctions result to be photoactive and their H_2 production follows the reactivity sequence of the noble metals: Pd>Pt>>Au, despite the metal loading.

Fig. 5a-c shows the cumulative evolution of H_2 for all 9 composites. In all cases activity scales with M loading, with diminishing returns as loadings reaches 2%. These results demonstrate that the M identity plays a key role, though noteworthy is the determination that Pd NPs enhance the H_2 production process more than either Au or Pt – previously only observed for single atom catalysts.[72] Hence, one can conclude that the intimate contact interface of the M and TiO_2, defined by the type of deposition, drives an efficient internal electronic communication via simple or numerous charge carrier pathways between the two moieties that ultimately leads to excellent, good or average photo activity.

By normalizing the H_2 results (**Fig. 5b**) with the mass of catalyst, the same trend as for the cumulative H_2 is observed for all samples, as expected. 2 wt.%Pd exhibits the highest HER rate, *ca.* 12.6 mmol g_{cat}^{-1} h^{-1}. In general, for all the Schottky junctions the normalized H_2

photoproduction rates are slightly higher compared with reported literature,[72–78] confirming that under comparable experimental conditions, the use of this compact reactor enhances the HER efficacy of the studied benchmark materials.

By comparing the cumulative HER curves (**Fig. 5c**) of only the higher M loadings, the Pd-loaded systems emerge as the most efficient, resulting in a production of 608 mL of H_2 in 3h, which (assuming a good stability over time) extrapolated temporally would produce 1L of H_2 after 2 continuous days. Contrastingly, for the Au junction, four days would be required to produce the same amount of H_2.

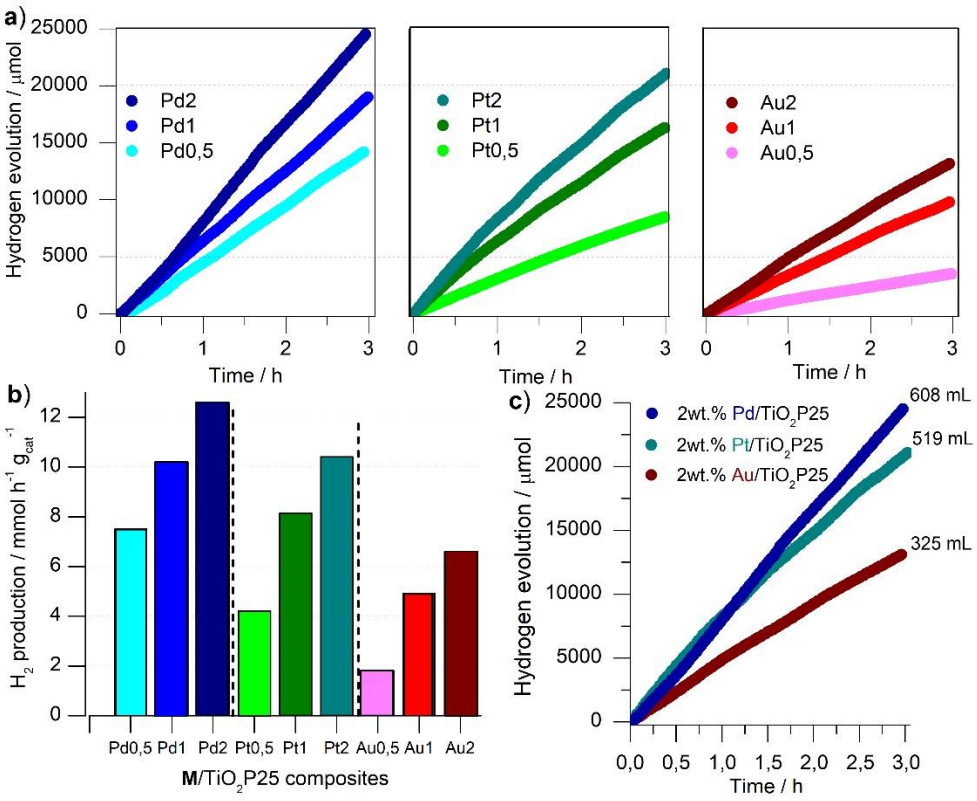

Figure 5. a) Cumulative evolution of hydrogen with 30 vol% of methanol under solar light (15.5 mW cm^{-2}) for the 0.5, 1 and 2 wt.% (Pd, Pt, and Au)/TiO_2 Schottky junctions **b)** Mean hydrogen formation rate per hour per mass **c)** Cumulative evolution of hydrogen of 2 wt.% (Pd, Pt, and Au)/TiO_2 composites with their equivalent liquid hydrogen production.

Table 2 contains a comparison of semi-equivalent Schottky systems from literature, tested in different reactors to contextualize the H_2 photoproduction results of this study. The M-based composites are also anchored in TiO_2, not necessarily P25 but anatase, rutile, brookite, or a combination of the mentioned. Here we focus on two efficiency factors, *ca.* HER production and Q.Y. per support (TiO_2). Material modification and reactor conditions are described in order to somewhat contextualize the provided data. The (Pd, Pt, Au)/TiO_2 Schottky junctions exhibit H_2 production rates slightly higher than previous studies, with quantum yields almost 2-fold higher than reported studies. These results demonstrate that the proposed novel geometry of the photoreactor improves the overall photonic, heat, and mass profiles, lowering the contributions due to loss processes.

Table 2. Comparison of photocatalytic efficiency for the TiO_2-based materials tested at similar reactor experimental conditions.

Efficiency		TiO_2 material			Reactor conditions				Ref.
HER mmol h^{-1} g_{cat}^{-1}	Q.Y.	M	%	Method	S. Agent	%	Lamp	Time h	
12.6	12.3	Pd	2	-	MeOH	30	500 W	3	Ours
10.4	10.1	Pt	2						
6.6	3.2	Au	2						
0.7	N.r.	Pd	1	-	MeOH	50	N.r.	5	[72]
2.2		Pt							
0.5		Au							
1.5	0.1	Au	0.3	Calcined	TEOA	1	150 W	2.5	[73]
3.0	1.7	Pd	1	Nb-doping, drying, calcined	MeOH	30	500 W	3	[75]
	2.0	Pt	1						
2.4	N.r.	Au	1	Calcined	MeOH	50	7.2 W	3	[76]
1.8	1.0	Pt	0.5	Calcined	MeOH	30	500 W	3	[77]
0.06	N.r.	Au	1	-	MeOH	50	1000 W	4	[78]

Cycling tests (**Fig. 6a**) were conducted with the highest-performing photocatalyst, 2% Pd/TiO_2. A decrease in activity in the cycles were calculated in the order of 26% decay. This considerable decrease may be associated with Pd NPs leaching,[79] impeding the initial co-catalytic function.

The local photonic absorption profiles (**Fig. 6b**) for the 2% samples reveal that Pt and Pd have a similar light absorption to that of TiO_2 P25, as expected and confirmed by the comparable UV-vis spectra. The 2%Au/TiO_2 however, increases its light absorption, essentially in front of the quartz window, enhancing capture efficacy of incoming photons compared with its Pd and Pt analogues. It is noteworthy to mention, that although the photons are the source of activation for the SC, this does not necessarily mean that all the absorbed photons will end up in useful excitons and from there separate charge-carriers that can transform the reacting molecules. To associate the photonic model implementation and the chemical conversion (H_2 photoproduction rate) the quantum yield is determined (**Fig. 6c**). The series of junctions follow the quantum yield (QY) sequence of the noble metals: Pd>Pt>>Au, in a linear trend with cumulative reactivity. Interestingly, the obtained QYs are notably higher compared with reported results[72–78] (at least double), verifying that for similar experimental conditions, the compact photoreactor enhances the mass/heat transport phenomena and exposure to light. Such enhancement favored transport-limited processes, resulting in a controlled assessment of the activity performance. In general, QY is found to be intrinsically related to metal content – with the exception of Au 2% (potentially due to diminishing enhancements from larger particle sizes). These results demonstrates that light absorption (density of absorbed photons) is not the only parameter influencing the material's activity[73] and that charge generation/separation/transport plays a key role. In addition, one cannot discount that accessibility to the active sites also dictates the efficiency of surface reactions. Therefore, this result paves the way to further questions regarding the quality of the interface between the Au NP

and their support. To this end, energy electron low spectroscopy (EELS, **Fig. 6d**) is carried out to better understand the mode/interaction present on a single Au NP and its support. The plasmon energy value is known to drastically depends on the electromagnetic environment of the NP that subtends it.[80] One single NP deposited on a substrate (TiO_2) is likely to exhibit dual energy modes: a plasmon mode localized at the substrate vicinity (evidencing the M/SC interface formation), another a plasmon mode localized at the vacuum interface. Eventually the mode localized at the vacuum NP interface (2.43±0.01 eV) is at a lower energy than the substrate contact mode (2.17±0.02 eV), resulting in a redshift. Consequently, the low energy mode is likely to increase with the increase in contact area, assuming homogeneous spherical NPs. The same trend is found in two isolated Au NPs for the 1%Au/TiO_2 sample (**Fig. S11**) that unexpectedly exhibit the same quantum yield as the 2% Au junction. Both Au NPs of 7.11 and 5.20 nm size display ΔPlasmon of (0.15 and 0.11) ±0.02 eV, which are (0.10 and 0.14) ±0.02 eV lower than the results for the 1%Au composite. This suggests that the Au NP -TiO_2 interface mode is of better quality in the 1%Au sample (of higher contact area) including a plasmon with a more pronounced oscillation. Such active surface plasmons can enhance two possible mechanisms either the intensification of the electromagnetic field towards the interior of the SC or the hot electron injection from the Au NP structure (visible photon capacity) to the conduction band of TiO_2 (UV photon limited).[49,64,81]

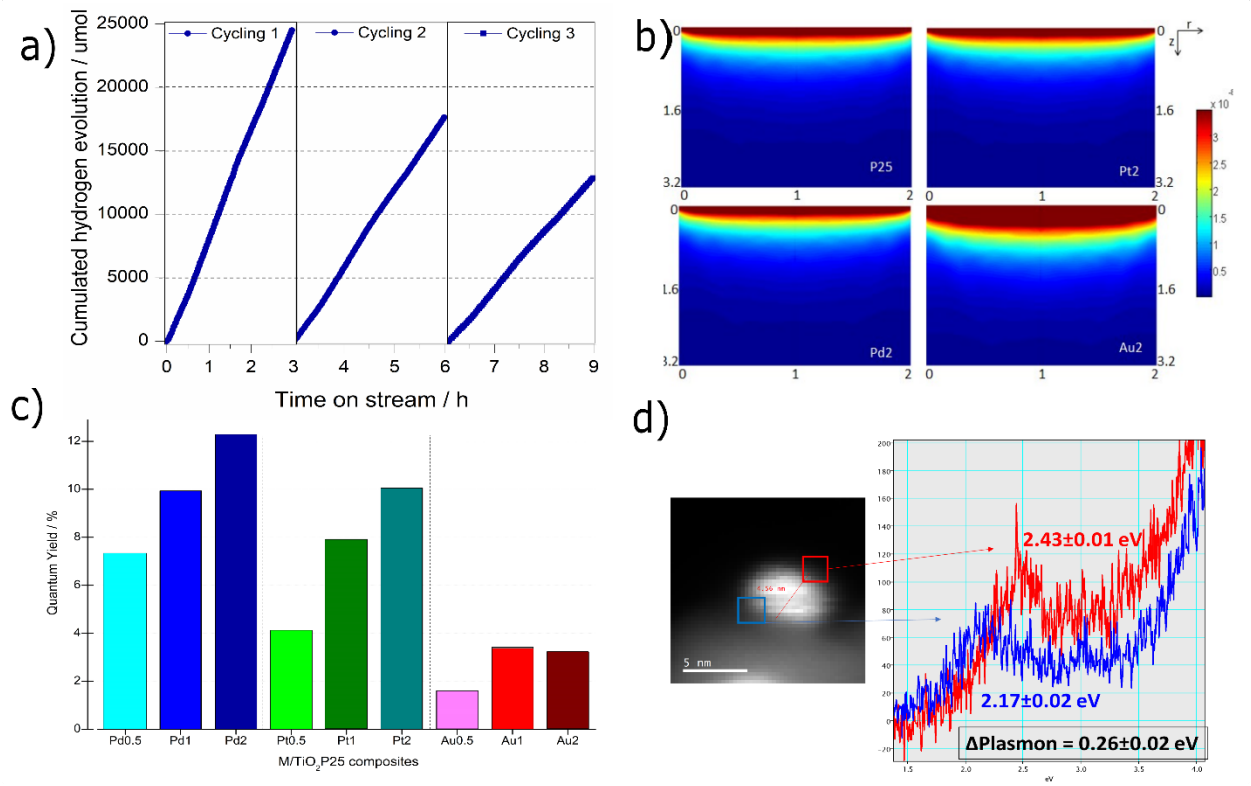

Figure 6. a) Cycling test of the highest-performing Schottky junction 2% Pd/TiO_2 with 30 vol% of methanol under solar light. **b)** Local volumetric rate of photon absorption (Einstein cm^{-3} s^{-1}) of the catalytic suspension obtained for samples Pt2, Pd2 and Au2 and TiO_2 P25 reference. Local 2D photonic profile obtained for each r and z position. **c)** Quantum yield results of all the composites. **d)** EELS analysis on a 4.56 nm Au NP exhibiting its plasmon energy and modes on the 1%Au/TiO_2 junction.

4. Conclusions

In summary, we have developed a new compact reactor dedicated to HER under standard experimental conditions that has been evaluated using Schottky (Pd, Pt, Au)/TiO_2 (as well-established materials in photocatalysis). H_2 photoproduction rates and quantum yields are almost one- and two-fold higher than literature average values, respectively, putting into evidence that the geometry and configuration setup brings the system one step closer to the ideal heat/mass/photonic profile, with low losses. The Schottky composites allow building novel structure-activity correlations. Insightful evidence is shown for the Au plasmon by coupling HRTEM, EELS, and UV-vis for the first time in literature, to the best of our knowledge. We stress two major conclusions: (A) the need for further development of compact and portable reactors to allow *in-situ* testing and coupling with key techniques such as TEM, XAS, XRD, among others and (B) the

reporting of homogeneous criteria (IUPAC) for the accurate comparison of efficiencies across different studies and groups. We propose the use of this new photoreactor as a benchmark to foster further progress in process and chemical engineering, accelerate the TRL, and as a strategy to overcome current limitations in scaling up photocatalysis.

5. Acknowledgements

EP and PJC acknowledge the financial support of the French ANR agency (ANR) under grant agreement ANR-18-CE09-0001 (C3PO) and the CNRS through the International Emerging Actions program (no. 08216). The results used the Imagerie-Gif core facility supported by l'Agence Nationale de la Recherche (ANR-11-EQPX-0029/Morphoscope, ANR-10-INBS-04/FranceBioImaging; ANR-11-IDEX-0003-02/ Saclay Plant Sciences). The X-ray photoelectron (XPS) data collection was performed at the EPSRC National Facility for XPS ("HarwellXPS"), operated by Cardiff University and UCL, under Contract No. PR16195. The authors acknowledge financial support from the CNRS-CEA "METSA" French network (FR CNRS 3507) on the platform STEM-LPS. This work has received support from the French State through the National Agency for Research under the program of future investment EQUIPEX TEMPOS-CHROMATEM with the reference ANR-10-EQPX-50. The authors thank Stéphane Cabaret (LPS/CNRS, Orsay) for the design and realization of the photoreactor, Anne Boos (IPHC/ECPM, Strasbourg) for the ICP-AES analyses and Fabrice Gros (CNRS/U. Clermont Ferrand) for fruitful reactor details discussions.

6. References

[1] I.E.A. (IEA), Stat. Rep. (2016) 24, 80.

[2] R. Perez, M. Perez, Int. Energy Agency Sol. Heat. Cool. Program. Sol. Updat. 50 (2009) 4–

5.

[3] P. Kruger, Int. J. Hydrogen Energy 30 (2005) 1515–1522.

[4] MIT Energy Initiat. (2015).

[5] N.S. Lewis, G. Crabtree, A.J. Nozik, M.R. Wasielewski, P. Alivisatos, H. Kung, J. Tsao, E. Chandler, W. Walukiewicz, M. Spitler, R. Ellingson, R. Overend, J. Mazer, M. Gress, J. Horwitz, C. Ashton, B. Herndon, L. Shapard, R.M. Nault, Basic Research Needs for Solar Energy Utilization. Report of the Basic Energy Sciences Workshop on Solar Energy Utilization, April 18-21, 2005, 2005.

[6] K. Takanabe, ACS Catal. 7 (2017) 8006–8022.

[7] M. Melchionna, P. Fornasiero, ACS Catal. 10 (2020) 5493–5501.

[8] I.E.A. (IEA), Technology Roadmap Hydrogen and Fuel Cells, 2015.

[9] A. Fujishima, K. Honda, Nature 238 (1972) 37–38.

[10] A. Kudo, Y. Miseki, Chem. Soc. Rev. 38 (2009) 253–78.

[11] F. Guzman, S.S.C. Chuang, C. Yang, Ind. Eng. Chem. Res. 52 (2013) 61–65.

[12] A. Primo, A. Corma, H. García, Phys. Chem. Chem. Phys. 13 (2011) 886–910.

[13] Y. Shiraishi, N. Yasumoto, J. Imai, H. Sakamoto, S. Tanaka, S. Ichikawa, B. Ohtani, T. Hirai, Nanoscale 9 (2017) 8349–8361.

[14] D. Ollis, P. Pichat, N. Serpone, Appl. Catal. B Environ. 99 (2010) 377.

[15] K. Nakata, A. Fujishima, J. Photochem. Photobiol. C Photochem. Rev. 13 (2012) 169–189.

[16] K.C. Christoforidis, P. Fornasiero, ChemCatChem 11 (2019) 368–382.

[17] K. Connelly, A.K. Wahab, H. Idriss, Mater. Renew. Sustain. Energy 1 (2012) 1–12.

[18] Y. Pellegrin, F. Odobel, Comptes Rendus Chim. 20 (2017) 283–295.

[19] J.T. Schneider, D.S. Firak, R.R. Ribeiro, P. Peralta-Zamora, Phys. Chem. Chem. Phys. 22 (2020) 15723–15733.

[20] H. El Marouazi, P. Jiménez-Calvo, E. Breniaux, C. Colbeau-Justin, I. Janowska, V. Keller, ACS Sustain. Chem. Eng. 9 (2021) 3633–3646.

[21] J. Li, P. Jiménez-Calvo, E. Paineau, M.N. Ghazzal, Catalysts 10 (2020) 89.

[22] Y. Wang, A. Vogel, M. Sachs, R. Sebastian Sprick, L. Wilbraham, S.J. A Moniz, R. Godin, M.A. Zwijnenburg, J.R. Durrant, A.I. Cooper, J. Tang, Nat. Energy 4 (2019) 746–760.

[23] K.P. Sundar, S. Kanmani, Chem. Eng. Res. Des. 154 (2020) 135–150.

[24] M. Isaacs, J. Garcia-Navarro, W.-J. Ong, P. Jiménez-Calvo, Glob. Challenges (2022) 2200165.

[25] M.J. Muñoz-Batista, M.M. Ballari, A. Kubacka, O.M. Alfano, M. Fernández-García, Chem. Soc. Rev. 48 (2019) 637–682.

[26] M.J. Muñoz-Batista, D. Rodríguez-Padrón, A.R. Puente-Santiago, A. Kubacka, R. Luque, M. Fernández-García, ChemPhotoChem 2 (2018) 870–877.

[27] A.A. Khan, M. Tahir, J. CO2 Util. 29 (2019) 205–239.

[28] J. Low, J. Yu, M. Jaroniec, S. Wageh, A.A. Al-Ghamdi, Adv. Mater. 29 (2017).

[29] R. Marschall, Adv. Funct. Mater. 24 (2014) 2421–2440.

[30] P. Jiménez-Calvo, V. Caps, V. Keller, Renew. Sustain. Energy Rev. 149 (2021) 111095.

[31] B. O'Regan, M. Grätzel, Nature 353 (1991) 737–740.

[32] W. Schottky, Naturwissenschaften 1938 2652 26 (1938) 843–843.

[33] D.B. Ingram, S. Linic, J. Am. Chem. Soc. 133 (2011) 5202–5205.

[34] M. Wang, M. Ye, J. Iocozzia, C. Lin, Z. Lin, M. Wang, J. Iocozzia, Z. Lin, C. Lin, M. Ye, Adv. Sci. 3 (2016) 1600024.

[35] Z.H.N. Al-Azri, W.-T. Chen, A. Chan, V. Jovic, T. Ina, H. Idriss, G.I.N. Waterhouse, J. Catal. 329 (2015) 355–367.

[36] W.T. Chen, A. Chan, Z.H.N. Al-Azri, A.G. Dosado, M.A. Nadeem, D. Sun-Waterhouse, H. Idriss, G.I.N. Waterhouse, J. Catal. 329 (2015) 499–513.

[37] Z.H.N. Al-Azri, V. Jovic, W.T. Chen, D. Sun-Waterhouse, J.B. Metson, G.I.N. Waterhouse, Int. J. Nanotechnol. 11 (2014) 695–703.

[38] J.J. Velázquez, R. Fernández-González, L. Díaz, E. Pulido Melián, V.D. Rodríguez, P. Núñez, J. Alloys Compd. 721 (2017) 405–410.

[39] J.C. Colmenares, A. Magdziarz, M.A. Aramendia, A. Marinas, J.M. Marinas, F.J. Urbano,

J.A. Navio, Catal. Commun. 16 (2011) 1–6.

[40] V.M. Daskalaki, P. Panagiotopoulou, D.I. Kondarides, Chem. Eng. J. 170 (2011) 433–439.

[41] B.S. Huang, F.Y. Chang, M.Y. Wey, Int. J. Hydrogen Energy 35 (2010) 7699–7705.

[42] J.J. Brancho, B.M. Bartlett, Chem. Mater. 27 (2015) 7207–7217.

[43] A. Kubacka, M. Fernández-García, G. Colón, Chem. Rev. 112 (2011) 1555–1614.

[44] X. Chen, C. Li, M. Grätzel, R. Kostecki, S.S. Mao, Chem. Soc. Rev. 41 (2012) 7909.

[45] M.K. Nazeeruddin, E. Baranoff, M. Grätzel, Sol. Energy 85 (2011) 1172–1178.

[46] S. Bai, N. Zhang, C. Gao, Y. Xiong, Nano Energy (n.d.).

[47] O. Ola, M.M. Maroto-Valer, J. Photochem. Photobiol. C Photochem. Rev. 24 (2015) 16–42.

[48] M. Rycenga, C.M. Cobley, J. Zeng, W. Li, C.H. Moran, Q. Zhang, D. Qin, Y. Xia, Chem. Rev. 111 (2011) 3669–712.

[49] Y. Dubi, Y. Sivan, Light Sci. Appl. 8 (2019) 2047–7538.

[50] S. Trasatti, J. Electroanal. Chem. Interfacial Electrochem. 39 (1972) 163–184.

[51] R. Parsons, Trans. Faraday Soc. 54 (1958) 1053–1063.

[52] G. Dahi, A. Eskandari, J. Dauchet, F. Gros, M. Roudet, J.-F. Cornet, Chem. Eng. Process. Process Intensif. 98 (2015) 174–186.

[53] M. Schwarze, D. Stellmach, M. Schröder, K. Kailasam, R. Reske, A. Thomas, R. Schomäcker, Phys. Chem. Chem. Phys. 15 (2013) 3466–3472.

[54] P. Jiménez-Calvo, C. Marchal, T. Cottineau, V. Caps, V. Keller, J. Mater. Chem. A 7 (2019).

[55] E. Paineau, G. Monet, V. Peyre, C. Goldmann, S. Rouzière, P. Launois, Langmuir (n.d.).

[56] C.D. Wagner, L.E. Davis, M. V. Zeller, J.A. Taylor, R.H. Raymond, L.H. Gale, Surf. Interface Anal. 3 (1981) 211–225.

[57] R.L. Romero, O.M. Alfano, A.E. Cassano, Ind. Eng. Chem. Res. 36 (1997) 3094–3109.

[58] J.J. Duderstadt, W.R. Martin, Transport Theory, John Wiley & Sons, New York, 1979.

[59] S. Hosseinpour, F. Tang, F. Wang, R.A. Livingstone, S.J. Schlegel, T. Ohto, M. Bonn, Y. Nagata, E.H.G. Backus, J. Phys. Chem. Lett. 8 (2017) 2195–2199.

[60] J. Of, N.-A.E.P.Ж.H.-T.E. Фізики, Том 9 (2017) 4005.

[61] P. Praveen, G. Viruthagiri, S. Mugundan, N. Shanmugam, Spectrochim. Acta Part A Mol. Biomol. Spectrosc. 117 (2014) 622–629.

[62] B. Ohtani, O.O. Prieto-Mahaney, D. Li, R. Abe, J. Photochem. Photobiol. A Chem. 216 (2010) 179–182.

[63] K. Masao, I. Okura, Photocatalysis: Science and Technology, I, Springer, Berlin, Heidelberg, 2002.

[64] P.I. Jiménez-Calvo, Synthesis, Characterization, and Performance of g-C3N4 Based

Materials Decorated with Au Nanoparticles for (Photo) Catalytic Applications, Université de Strasbourg, 2019.

[65] N. Li, P. Zhao, D. Astruc, Angew. Chemie - Int. Ed. 53 (2014) 1756–1789.

[66] M. Pourbaix, Atlas of Electrochemical Equilibria in Aqueous Solutions, [1st English ed.]., Pergamon Press, Oxford ;New York, 1966.

[67] K.L. Kelly, E. Coronado, L.L. Zhao, G.C. Schatz, (2003).

[68] S. Linic, P. Christopher, D.B. Ingram, Nat. Mater. 10 (2011) 911–921.

[69] M. Bingham, A. Mills, J. Photochem. Photobiol. A Chem. 389 (2020) 112257.

[70] H.B. Michaelson, J. Appl. Phys. 21 (1950) 536–540.

[71] M.G. Sanchez, J.L. Gazquez, J. Catal. 104 (1987) 120–135.

[72] G. Cha, I. Hwang, S. Hejazi, A.S. Dobrota, I.A. Pašti, B. Osuagwu, H. Kim, J. Will, T. Yokosawa, Z. Badura, Š. Kment, S. Mohajernia, A. Mazare, N. V. Skorodumova, E. Spiecker, P. Schmuki, IScience 24 (2021) 102938.

[73] P. Jiménez-Calvo, V. Caps, M.N. Ghazzal, C. Colbeau-Justin, V. Keller, Nano Energy 75 (2020) 104888.

[74] M.J. Muñoz-Batista, D. Motta Meira, G. Colón, A. Kubacka, M. Fernández-García, Angew. Chemie Int. Ed. 57 (2018) 1199–1203.

[75] U. Caudillo-Flores, M.J. Muñoz-Batista, M. Fernández-García, A. Kubacka, Appl. Catal. B Environ. 238 (2018) 533–545.

[76] J.B. Priebe, J. Radnik, A.J.J. Lennox, M.-M. Pohl, M. Karnahl, D. Hollmann, K. Grabow, U. Bentrup, H. Junge, M. Beller, A. Brückner, ACS Catal. 5 (2015) 2137–2148.

[77] O. Fontelles-Carceller, M.J. Muñoz-Batista, J.C. Conesa, M. Fernández-García, A. Kubacka, Appl. Catal. B Environ. (2017).

[78] J. Nie, J. Schneider, F. Sieland, L. Zhou, S. Xia, D.W. Bahnemann, RSC Adv. 8 (2018) 25881–25887.

[79] M. Altomare, N.T. Nguyen, S. Hejazi, P. Schmuki, Adv. Funct. Mater. 28 (2018) 1704259.

[80] M. Kociak, O. Stéphan, Chem. Soc. Rev. 43 (2014) 3865–3883.

[81] D.C. Ratchford, ACS Nano 13 (2019) 13610–13614.